

Contribution for the JETP special issue in honor of L.V. Keldysh's 85th birthday

Collective Phenomena in Cold Indirect Excitons¹

L. V. Butov

Department of Physics, University of California at San Diego, La Jolla, CA 92093-0319, USA

e-mail: lvbutov@physics.ucsd.edu

Received August 11, 2015

Abstract—Due to their long lifetimes, indirect excitons can cool to below the temperature of quantum degeneracy. This gives an opportunity to experimentally study cold composite bosons. Both theoretically predicted phenomena and phenomena that have not been anticipated were observed in a cold gas of indirect excitons. In this contribution, we overview our studies of cold indirect excitons over the past decade, presenting spontaneous coherence and condensation of excitons, spatially modulated exciton state, long-range spin currents and spin textures, and exciton localization—delocalization transitions.

DOI: 10.1134/S1063776116030031

1. INTRODUCTION

An exciton is a bound pair of an electron and a hole. At densities $n \lesssim 1/a_B^D$, excitons are hydrogen-like composite Bose particles [1] (a_B is the exciton Bohr radius and D the dimensionality). Since the temperature of quantum degeneracy scales inversely with the mass, and the exciton mass is small, typically smaller than the free electron mass, the quantum degeneracy in exciton gases can be achieved at temperatures of about 1 K [1], orders of magnitude higher than μK temperatures for atoms [2, 3] and available in helium refrigerators. Theoretical predictions for cold exciton and electron-hole systems include a variety of collective states, such as a Bose–Einstein condensate [1], BCS-like condensate [4], paired Laughlin liquid [5], coupled Wigner solids [5], and excitonic charge-density wave [6].

The experimental realization of a cold exciton gas with the exciton temperature $T_X \sim 1$ K requires a system where the exciton lifetime is sufficiently long such that excitons can cool to low temperatures before recombination. Besides, the realization of a cold and dense exciton gas requires the semiconductors in which an excitonic state is the ground state and, in particular, has lower energy than the metallic electron-hole liquid. The latter is the ground state in Ge and Si, which forms an obstacle for creating cold and dense exciton gases in these materials [7]. Studies of various materials indicate that the experimental realization of a cold exciton gas is challenging [8–16].

Cold and dense exciton gases with $T_X \ll 1$ K are realized in a system of indirect excitons. An indirect exciton (IX) is a bound pair of an electron and a hole in separated quantum well (QW) layers [17–19] (Figs. 1a, 1b). The lifetime of IXs is long due to the spatial separation between electrons and holes. In coupled QW (CQW) samples, which we study, the lifetime of IXs is controlled by voltage typically in the range from a few tens of ns to a few μs , orders of magnitude longer than the lifetime of regular direct excitons, which is in the range of a few tens of ps in GaAs QWs [20–22]. Furthermore, IX cooling is fast due to relaxation of the momentum conservation law in the direction perpendicular to the QW plane [23, 24]. The long lifetime and fast energy relaxation allow the IXs in GaAs structures CQWs to cool down to ~ 0.1 K within their lifetime [25], well below the temperature of quantum degeneracy $T_0 = 2\pi\hbar^2 n/m \approx 3$ K for the exciton density per spin state $n = 10^{10}$ cm^{-2} and the exciton mass $m = 0.22m_0$ relevant to the experiments.

The realization of cold exciton gases using IXs gives an opportunity to study low-temperature exciton states. IXs were studied in a number of experiments [25–65]. The findings in cold IX gases include a spontaneous transition into a spatially modulated exciton state [26, 32, 41], spontaneous coherence and condensation of excitons [27–30, 32], long-range spin currents and spin textures [31, 32], perfect Coulomb drag [33], enhanced exciton radiative recombination [35], enhanced exciton tunneling recombination [36, 37], and enhanced exciton scattering to low-energy states [25]. Some of the observed phenomena, like spontaneous coherence and condensation, were predicted

¹The article is published in the original.

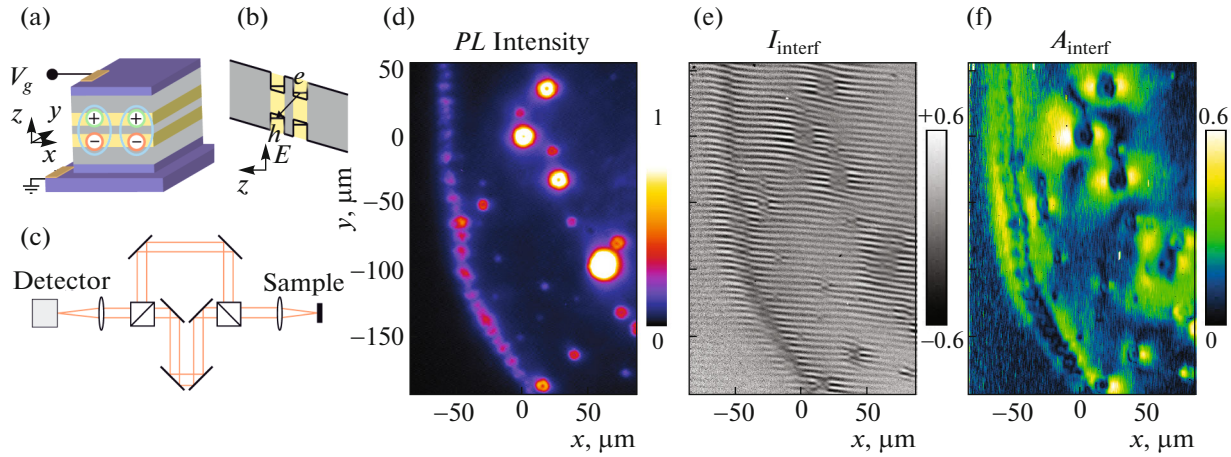


Fig. 1. (Color online) (a) Diagram of a CQW structure: n^+ -GaAs (blue), $\text{Al}_{0.33}\text{Ga}_{0.67}\text{As}$ (grey), GaAs quantum well (yellow). V_g is the applied voltage. Ellipses indicate IXs composed of electrons (–) and holes (+). (b) CQW band diagram; e , electron; h , hole; E , energy. The arrow indicates an IX. (c) Diagram of the interferometric setup. (d) IX emission pattern. (e) Interference pattern $I_{\text{interf}}(x, y)$ for $\delta x = 2 \mu\text{m}$. (f) Pattern of the amplitude of the interference fringes $A_{\text{interf}}(x, y)$, presenting a map of coherence. The temperature in the refrigerator at the sample is $T_{\text{bath}} = 0.1 \text{ K}$. From [29].

theoretically [1] and some of them, like spontaneous transition into a spatially modulated exciton state, were found experimentally in a cold IX gas. In this contribution, we briefly overview our studies of IXs over the past decade, presenting spontaneous coherence and condensation of excitons, spatially modulated exciton state, long-range spin currents and spin textures, and exciton localization-delocalization transitions. We also briefly present excitonic devices that allow IX control.

2. SPONTANEOUS COHERENCE IN A COLD EXCITON GAS

Spontaneous coherence of matter waves is equivalent to condensation of particles in momentum space. The Fourier transform of the first-order coherence function $g_1(\delta x)$ gives the particle distribution n_q in the momentum space. In turn, the width of $g_1(\delta x)$, the coherence length ξ , is inversely proportional to the width of n_q . In a classical gas at thermal equilibrium with n_q given by the Maxwell–Boltzmann distribution, ξ is close to the thermal de Broglie wavelength $\lambda_{dB} = (2\pi\hbar^2/mT)^{1/2}$ and is typically small ($\lambda_{dB} \sim 0.5 \mu\text{m}$ for IX with $m = 0.22m_0$ at $T = 0.1 \text{ K}$). In a Bose–Einstein condensate with narrow n_q , $g_1(\delta x)$ is broad and the coherence length is much larger than in a classical gas, $\xi \gg \lambda_{dB}$. The measurement of spontaneous coherence with $\xi \gg \lambda_{dB}$ is the direct measurement of a Bose–Einstein condensate with narrow n_q . In this section, we overview the measurements of IX spontaneous coherence reported in [29].

In earlier studies, evidence for spontaneous coherence was obtained for IXs in CQWs [35] and for IXs in quantum Hall bilayers [36, 37]. In these experiments,

the onset of spontaneous coherence was respectively evidenced by a strong enhancement of exciton radiative recombination [35] and exciton tunneling recombination [36, 37]. Radiative recombination rate increases with the coherence length for QW excitons [20, 21] and an increase in the coherence length at exciton condensation leads to an enhancement of exciton radiative recombination [66]. The results of other transport and optical experiments were also consistent with spontaneous coherence of IXs [33–40]. However, no direct measurement of coherence was performed and no enhancement of exciton coherence length beyond the classical value was directly detected in these studies.

The recombining excitons transform to photons, which inherit their coherence properties: spontaneous coherence of excitons translates into coherence of the emitted light and can be studied by interferometry. Before work [29], we observed an enhancement of the IX coherence length well beyond λ_{dB} using a single-pinhole interferometric technique [27, 28]. However, this technique does not measure $g_1(\delta x)$ and the derivation of the exciton coherence length in [27, 28] was based on a mathematical analysis of the data. The interferometric experiments used in [29] probe the first-order coherence function and provide a direct measurement of the IX spontaneous coherence with $\xi \gg \lambda_{dB}$.

In [29], the pattern of the first-order coherence function $g_1(\delta x)$ was measured by shift interferometry: the emission images produced by each of the two arms of the Mach–Zehnder interferometer (Fig. 1c) were shifted with respect to each other to measure the interference between the emission of IXs spatially separated by δx . Spontaneous coherence was studied in the region of rings in the exciton emission pattern. Exciton

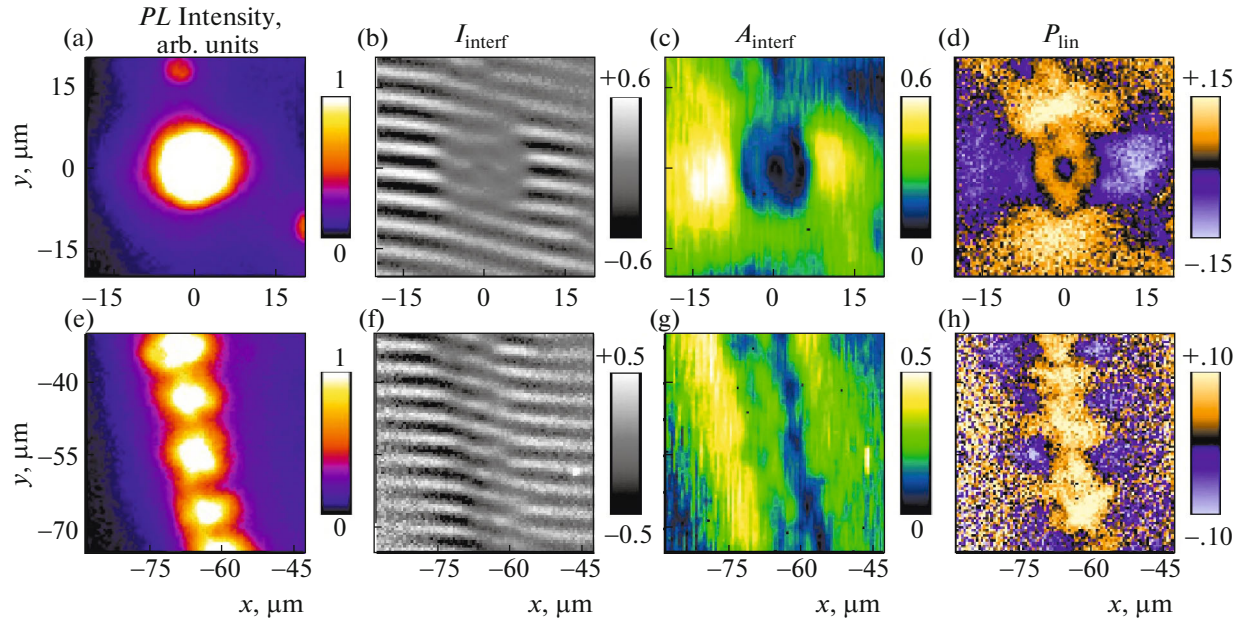


Fig. 2. (Color online) (a–d) A region of an LBS; (e–h) a region of the external ring. Shown are the IX emission pattern (a, e), the interference pattern at shift $\delta x = 2 \mu\text{m}$ (b, f), the amplitude $A_{\text{interf}}(x, y)$ of interference fringes (c, g), and the linear polarization of IX emission $P_{\text{lin}} = (I_x - I_y)/(I_x + I_y)$ (d, h). $T_{\text{bath}} = 0.1 \text{ K}$. From [29].

rings (including the inner ring, the external ring, and localized bright spot (LBS) rings) were observed earlier [26]; their origin is discussed in Section 3. In experiments [29], the photoexcitation was more than 400 meV above the energy of IXs, and the 10- μm -wide laser excitation spot was farther than 80 μm away from both the LBS and the external ring. Therefore, in the area of these rings, IX coherence forms spontaneously. Because of their separation from the laser spot, where excitons are heated due to optical excitation, the external and LBS rings are sources of cold excitons.

Figure 1d shows a segment of the IX emission pattern, with a section of the external ring and smaller LBS rings. The pattern of interference fringes is shown in Fig. 1e and the map of their amplitude, A_{interf} , in Fig. 1f. The quantity A_{interf} describes the degree of coherence of IXs, as detailed below. The regions of extended spontaneous coherence of IXs correspond to the green and yellow colors in Fig. 1f.

Figure 2 presents the patterns of coherence of IX emission in regions of an LBS and the external ring. The observed properties of IX coherence are qualitatively similar around both these sources of cold excitons. We first consider the LBS region. At low temperatures, a strong enhancement of A_{interf} is observed at a distance $r \sim r_0 = 7 \mu\text{m}$ from the LBS center (Figs. 2b, 2c). This enhancement of the degree of coherence shows the emergence of spontaneous coherence of excitons.

Figure 2d presents a pattern of linear polarization around an LBS. It spatially correlates with the pattern of the amplitude of the interference fringes A_{interf} :

compare Fig. 2c and 2d. At $r \gtrsim r_0$, a vortex of linear polarization with the polarization perpendicular to the radial direction is observed. Such polarization vortices are described in Section 4.

Close to the heating sources within the LBS ring, the exciton gas is hot and no spontaneous coherence forms there (the heating of the exciton gas is due to the current filament at the LBS center and the binding energy released at the exciton formation in the ring [43]). This is revealed by the small amplitude of the interference fringes. Excitons cool down with increasing the distance r from the heating sources and approach the condensation temperature. At $r = r_0$, the coherence degree sharply rises, indicating the emergence of spontaneous coherence of excitons. This is revealed by the strong enhancement of the amplitude of the interference fringes (Fig. 2c).

Similar phenomena are observed in the external ring region. At low temperatures, a spatially modulated exciton state called the macroscopically ordered exciton state (MOES) forms in the external ring [26] (Figs. 1d and 2e) and a periodic polarization texture forms around the periodic array of beads in the MOES (Fig. 2h). The MOES and periodic polarization texture are described in Sections 3 and 4. Figures 2f and 2g show spontaneous coherence of excitons observed in the MOES. It emerges at low temperatures, along with the spatial order of exciton beads and the periodic polarization texture.

We now discuss the measurements of the first-order coherence function. We measured the emission intensity I_1 for arm 1 open, I_2 for arm 2 open, and I_{12}

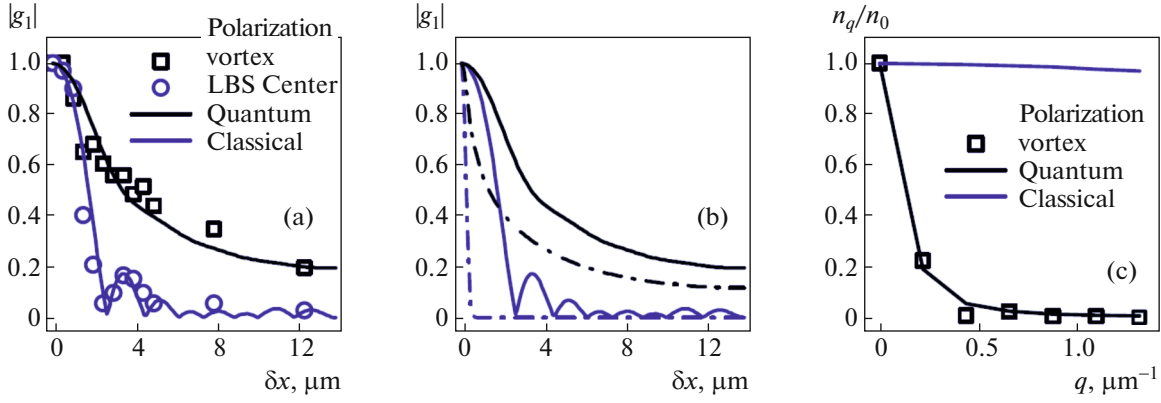


Fig. 3. (Color online) (a) Measured first-order coherence function $|g_1(\delta x)|$ for the polarization vortex (squares) and the LBS center (circles), and a simulated $|g_1(\delta x)|$ for a quantum (black line) and classical (blue line) gas. (b) Simulated $|g_1(\delta x)|$ for a quantum (black) and classical (blue) gas with (solid) and without (dashed) convolution with the PSF. (c) Distribution in momentum space obtained by the Fourier transform of g_1 in (b) for a quantum (black line) and a classical (blue line) gas. From [29].

for both arms open, and calculated the interference pattern $I_{\text{interf}} = [I_{12} - I_1 - I_2]/[2(I_1 I_2)^{1/2}]$. The first-order coherence function $g_1(\delta \mathbf{r})$ is given by the amplitude of the interference fringes $A_{\text{interf}}(\delta \mathbf{r})$ in “the ideal experiment” with perfect spatial resolution. In practice, the measured $A_{\text{interf}}(\delta \mathbf{r})$ is given by the convolution of $g_1(\delta \mathbf{r})$ with the point-spread function (PSF) of the optical system used in the experiment [28]. The PSF width corresponds to the spatial resolution of the optical system ($\sim 1.5 \mu\text{m}$ in our experiments).

The measurements of $A_{\text{interf}}(\delta x)$ in the polarization vortex and in the LBS center are presented in Fig. 3a. In the hot LBS center, A_{interf} quickly drops with δx and the shape $A_{\text{interf}}(\delta x)$ fits well to the PSF, which is shown by the blue line. In the polarization vortex, $g_1(\delta x)$ extends to large δx , demonstrating spontaneous coherence. A fit to the experimental points computed using a model described below is shown by the black line (Fig. 3a).

Figures 3b and 3c demonstrate the relation between the first-order coherence function $g_1(\delta x)$ and the particle distribution n_q in the momentum space. Figure 3b presents $g_1(\delta x)$ for a classical gas (blue dashed line) and for a quantum gas (black dashed line); both curves are for a spatially homogeneous gas of noninteracting particles with a quadratic dispersion. Both gases are at 0.1 K; the occupation number of the $q = 0$ momentum state (n_0) is $\ll 1$ for the classical gas, but is 5000 for the quantum gas. The convolution of these $g_1(\delta x)$ with the PSF produces data shown as black and blue solid lines, which respectively fit to $A_{\text{interf}}(\delta x)$ in the polarization vortex and in the LBS center (Figs. 3a, 3b). The Fourier transform of $g_1(\delta x)$ in Fig. 3b gives the momentum occupation factor n_q shown in Fig. 3c. Figure 3b and 3c illustrates that a classical gas is characterized by a broad distribution in momentum space n_q and a narrow $g_1(\delta x)$, whereas a quantum gas is characterized by

a narrow n_q and an extended $g_1(\delta x)$. For a classical gas, $g_1(\delta x)$ reduces substantially within λ_{dB} , which scales $\propto T^{-1/2}$ and is about $0.5 \mu\text{m}$ at 0.1 K. The extension of $g_1(\delta x)$ well beyond λ_{dB} indicates a coherent exciton state.

Figure 3a also illustrates why $\delta x = 2 \mu\text{m}$ is selected or mapping extended spontaneous coherence of excitons. The shift $\delta x = 2 \mu\text{m}$ is chosen to exceed both λ_{dB} and the PSF width. At such δx , only weak coherence given by the PSF value at $\delta x = 2 \mu\text{m}$ can be observed for a classical gas. The regions of enhanced coherence exceeding such a background level reveal the regions with spontaneous coherence of excitons.

We measured the exciton interference pattern at different δr to produce the spatial map of $g_1(\delta r)$ and, in turn, ξ . Spontaneous coherence of IXs is observed in the polarization vortices and in the macroscopically ordered exciton state [29]. The coherence length in these regions is much larger than in a classical gas, $\xi \gg \lambda_{dB}$, indicating a coherent state with a much-narrower-than-classical exciton distribution in momentum space, characteristic of a condensate. The observed coherence length in the polarization vortex exceeds $\lambda_{dB} = 0.5 \mu\text{m}$ at 0.1 K by more than an order of magnitude [29]. The coherence length in the MOES is smaller than in the polarization vortex. This may be related to fluctuations of the exciton density wave in the external ring. Such fluctuations are considered in Section 3.

3. FLUCTUATION AND COMMENSURABILITY EFFECT OF THE EXCITON DENSITY WAVE

A spatially ordered excitonic state in which the exciton density undergoes modulational instability was observed in [26]. This state, dubbed the macroscopically ordered exciton state (MOES), exhibits

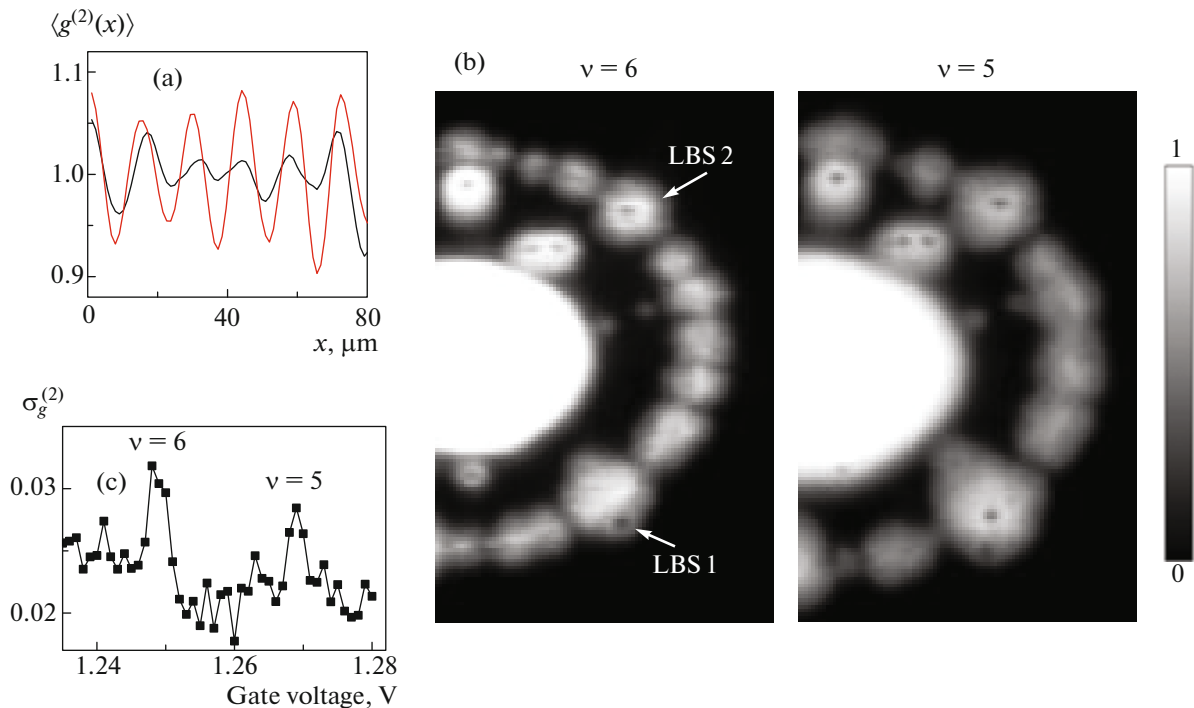


Fig. 4. (Color online) (a) The second-order correlation function $g^{(2)}$ for the IX emission intensity profile along the exciton density wave between LBS 1 and LBS 2 of length L (shown in (b)) with averaging over 27 second data acquisition movie. The commensurability numbers $\nu = L/\lambda_c$ are 7 (red) and 6.5 (black). (b) Images of the IX emission pattern are averaged over 27 s for different ν . Left (right) image shows six (five) wavelengths of the exciton density wave between LBS 1 and LBS 2. (c) Standard deviation of $g^{(2)}$ as a function of gate voltage, which controls the instability wavelength λ_c . For all data, V and P are varied simultaneously as in Fig. 5c such that the ring radius is fixed. The peaks indicate the suppression of phase fluctuations of the exciton density wave at integer ν . From [41].

approximately periodic spatial modulation within an exciton ring. The MOES forms when the IX gas is cooled below a few Kelvin close to the temperature of quantum degeneracy. The MOES occurrence initiated intensive experimental [27, 29, 32, 41, 43, 44] and theoretical studies [67–74]. The following MOES properties were revealed in the experiments. (i) The IX coherence length ξ in the MOES reaches microns [27, 29, 32], an order of magnitude greater than in a classical exciton gas, showing that the MOES is a condensate in momentum space. This property was reviewed in Section 2. (ii) The MOES forms in the external ring of the exciton pattern formation [26]. The external ring itself forms on the interface between the electron-rich and hole-rich regions [43, 45, 75–77]. This interface is essential for the MOES since no spontaneous density modulation is observed in another exciton ring—the inner ring, which forms due to IX transport and cooling, and where no such an interface is involved [26, 42]. (iii) The MOES is characterized by repulsive IX interaction [44]. This is consistent with the predicted repulsive interaction between the IXs [5, 78, 79], which are dipoles with a built-in dipole moment $\sim ed$, where d is the distance between the electron and hole layers. Repulsive interaction results in a monotonic enhancement of the IX energy with

density [34] and forms a negative feedback to density fluctuations, thus acting against density modulation. A positive feedback to density fluctuation leading to a spontaneous density modulation and consistent with the measured properties of the MOES is needed to explain the MOES origin. A search for a mechanism responsible for the formation of the MOES had led to a model attributing an instability to stimulated processes of exciton formation at the interface between the electron-rich and hole-rich regions that build up near quantum degeneracy [68].

In this section, we overview the recently observed fluctuations of the exciton density wave and the commensurability effect. The fluctuations are suppressed when the number ν of wavelengths of the exciton density wave confined between defects is an integer [41]. This phenomenon is presented in Fig. 4c. As is detailed in what follows, the suppression of fluctuations of the exciton density wave at integer ν is revealed by pronounced maxima in the standard deviation of the second-order correlation function for the IX emission intensity profile along the exciton density wave between defects. We also analyzed the stability of the exciton density wave by numerical simulations and found the commensurability effect within the model

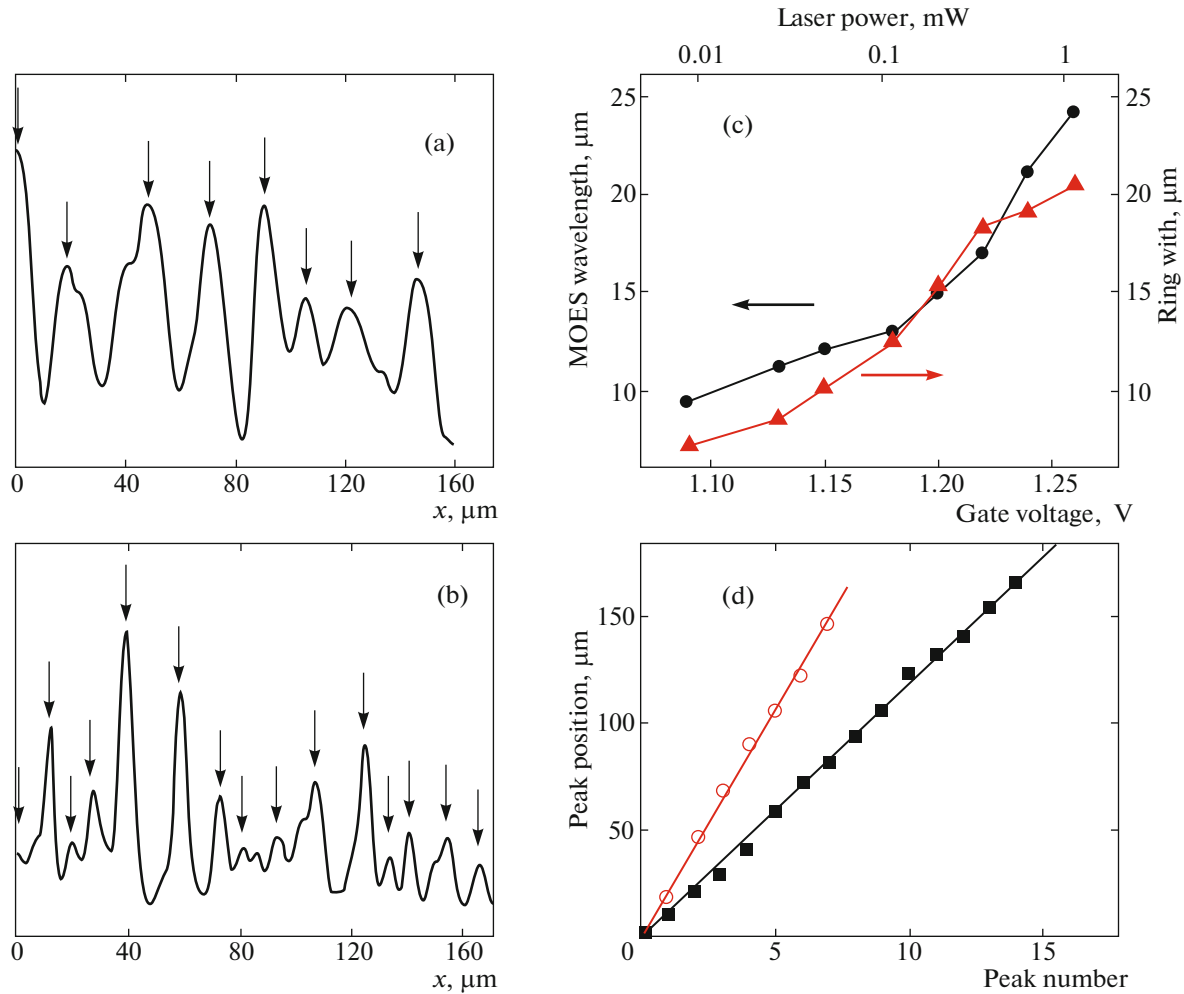


Fig. 5. (Color online) (a, b) The IX emission intensity profile along a segment of the external exciton ring for different V and P . (c) The MOES wavelength λ_c (points) and the ring width δ_r (triangles) vs V and P . (d) The MOES bead position vs the peak number for the ring segment in (a) (circles) and (b) (squares). For all data, V and P are varied simultaneously such that the ring radius is fixed. From [41].

describing the exciton density wave in terms of an instability due to stimulated processes.

Previous studies have shown that increasing the laser excitation power P leads to the increase in the external ring radius due to the enhancement of the hole source, while increasing the applied gate voltage V leads to a decrease in the ring radius due to the enhancement of the electron source [43, 45, 75–77]. In this section, we overview recent experiments where P and V are varied simultaneously such that the ring radius and position are kept constant [41]. The simultaneous increase of P and V leads to the enhancement of both electron and hole sources and, as a result, the exciton density in the ring. Figure 5c shows that increasing the exciton density leads to an increase in the MOES wavelength λ_c . MOES beads are essentially equidistant, forming an ordered array, while the bead intensities vary from bead to bead (Figs. 5a, 5b, 5d). We refer to such a quasiperiodic array as the excitonic

density wave. λ_c is controlled by P and V within the range 9–24 μm for the experiments in Fig. 5. λ_c up to 40 μm were achieved for other ring radii set by other values of P and V . Figure 5c also shows that increasing the exciton density leads to an increase in the ring width δ_r , along with an increase in the MOES wavelength λ_c .

The exciton pattern formation includes localized bright spots (LBS), which are associated with defects—electron current filaments in the sample [43]. Figure 6 shows that LBS beads are stable while MOES beads fluctuate with time. Both these fluctuations (Fig. 6c) and λ_c variation with density for a fixed ring position (Fig. 5c) indicate that the exciton density modulation in the MOES forms spontaneously rather than due to the in-plane disorder.

The stability of LBS beads and fluctuations of MOES beads (Fig. 6) show that the phase of the exci-

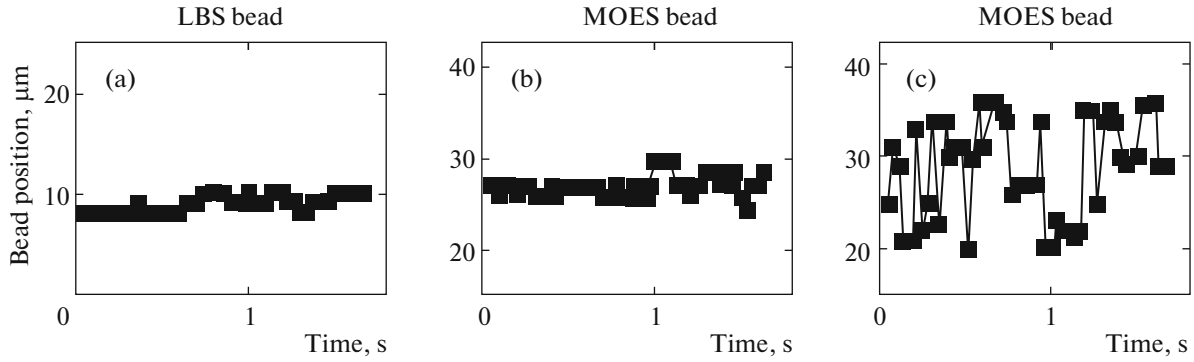


Fig. 6. Positions of (a) an LBS bead and a MOES bead for (b) integer v and (c) noninteger v vs time. From [41].

ton density wave is locked at LBS defects and fluctuates in between them. Controlling the exciton density in the ring (by varying P and V) allows probing the fluctuations of the exciton density wave for different ratios between the MOES wavelength λ_c and the length L of the ring segment between two LBS on the ring (such as LBS 1 and LBS 2 in Fig. 4b). The amplitude of the fluctuations is small when the number of wavelengths of the exciton density wave confined between the defects $v = L/\lambda_c$ is an integer. In turn, fluctuations increase for noninteger v (compare Fig. 6c presenting large fluctuations at noninteger v with Fig. 6b presenting smaller fluctuations at integer v). The LBS bead positions are stable for any v in adjacent ring segments.

This commensurability effect is quantified in Fig. 4c, which presents the standard deviation $\sigma_{g^{(2)}}$ of the second-order correlation function

$$g^{(2)}(x) = \frac{\langle I(x')I(x'+x) \rangle}{\langle I(x') \rangle^2}$$

for the IX emission intensity profile $I(x)$ along the exciton density wave between LBS 1 and LBS 2. Apparently, a stable periodic wave produces strong oscillations in the $g^{(2)}(x)$ correlation function with the distance between the maxima corresponding to the wave period, while fluctuations of the wave smear out such oscillations. Figure 4a shows that stronger oscillations in $g^{(2)}(x)$ are observed at integer v . In turn, $\sigma_{g^{(2)}}$ gives a measure for the wave fluctuations: large values of $\sigma_{g^{(2)}}$ correspond to a stable periodic wave, while small values of $\sigma_{g^{(2)}}$ correspond to stronger fluctuations that smear out the periodic wave structure. Figure 4c shows pronounced maxima in $\sigma_{g^{(2)}}$ indicating suppression of the fluctuations of the exciton density wave at integer v .

By developing a kinetic theory of the coupled electron-hole-exciton system, it has been shown that the transition into a spatially modulated state could be attributed to stimulated processes that build up near

quantum degeneracy [68]. The stimulated processes provide a positive feedback for density fluctuation, leading to spontaneous density modulation. This mechanism is consistent with the measured properties of the MOES outlined at the beginning of Section 3: (i) the MOES is a condensate in momentum space [27, 29, 32], (ii) the MOES forms in the external ring on the interface between the electron-rich and hole-rich regions [43, 45, 75–77], and (iii) the MOES is characterized by repulsive IX interaction [44].

The effects of commensurability on the stability of the exciton density wave and their potential role on fluctuations were addressed in [41]. Following [68], the starting point of the analysis in [41] relies on a transport theory involving a system of coupled nonlinear diffusion equations for the electron, hole, and exciton densities, with a local source for the holes (at the laser excitation spot) and a distributed source for electrons. In the steady state, the solution of these transport equations predicts the development of a ring of exciton density separating a hole-rich region within the ring from an electron-rich region outside the ring [43, 45, 75–77]. Further, by correlating the electron-hole binding rate with the exciton density consistent with the effects of stimulated processes that build near quantum degeneracy, it was shown that there is a type-II instability towards the development of a broken-symmetry state in which the electron/hole and exciton densities acquire a periodic modulation around the ring [68].

To assess the potential for collective fluctuations to drive the observed commensurability effect, the influence of spatial confinement on the stability of the modulated state was investigated following continuous changes in the value of a control parameter ζ [41]. For changing values of ζ , the steady-state configurations transit sequentially between configurations with integer values of v . When the natural wavelength of the instability translates to an integer v , the wavelength in the constrained ring geometry does not change within large variations in ζ , indicating that the exciton density wave is stable against fluctuations. However, when the

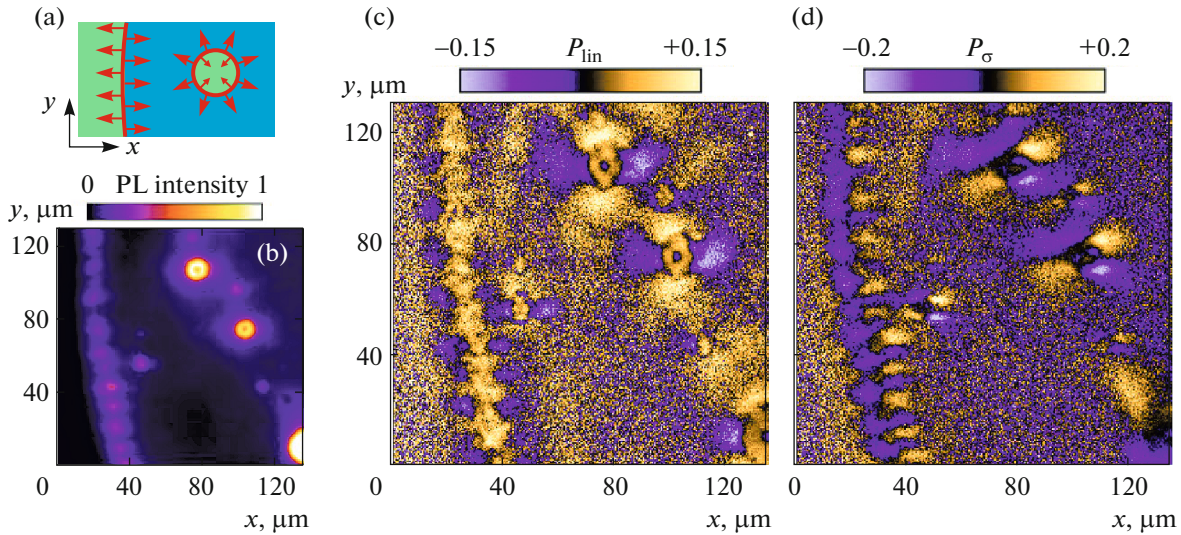


Fig. 7. (Color online) (a) Schematic of exciton formation in the external ring (left) and the LBS ring (right); excitons (red) form on the boundary of hole-rich (blue) and electron-rich (green) areas. IX transport is indicated by red arrows. (b) A segment of the IX emission pattern showing the external ring (left) and multiple LBS. (c, d) Patterns of linear $P_{\text{lin}} = (I_x - I_y)/(I_x + I_y)$ (c) and circular $P_{\sigma} = (I_{\sigma^+} - I_{\sigma^-})/(I_{\sigma^+} + I_{\sigma^-})$ (d) polarization of the IX emission in the region shown in (b). $T_{\text{bath}} = 0.1$ K. From [31].

natural wavelength translates to noninteger ν , the wavelength changes dramatically with small variations in ζ , indicating that the exciton density wave is unstable, consistently with the commensurability effect.

Finally, the observed enhancement of both the MOES wavelength λ_c and the ring width δ_r with density (Fig. 5c) is also consistent with the model. Indeed, within the model, both λ_c and δ_r increase with the diffusion length, which, in turn, increases with density due to screening on the in-plane disorder.

The MOES is a state with spontaneously broken symmetry involving a large number of excitons $\sim 10^6$ in the ring segment between LBS 1 and LBS 2 in Fig. 4). Earlier measurements described in Section 2 revealed that the coherence length in the MOES is much larger than in a classical exciton gas, identifying MOES as a quantum boson gas [27, 29, 32]. However, the coherence length in the MOES is limited by a few μm and is significantly shorter than the MOES wavelength ($\lambda_c \sim$ few tens of μm , see Fig. 5c). In contrast, the commensurability effect presents a collective behavior of the entire macroscopic system of IXs in the ring segment of the length ~ 100 μm containing several MOES wavelengths (Fig. 4b). This shows that the commensurability effect is a collective phenomenon in quantum boson gases.

4. SPIN CURRENTS IN A COHERENT EXCITON GAS

In this section, we overview the measurements of long-range spin currents and spin textures in a coherent gas of IXs around the exciton rings [31]. The latter

were presented in Sections 2 and 3. The spin currents result in the appearance of a variety of polarization patterns, including helical patterns, four-leaf patterns, spiral patterns, bell-like patterns, and periodic patterns. The long-range spin currents are based on a new mechanism for suppression of spin relaxation: the formation of a coherent gas of boson pairs, IXs, which produces a strong enhancement of electron and hole spin relaxation times.

The condensation of IXs was predicted to cause the suppression of exciton scattering [17]. The coherent transport of IXs over macroscopic lengths $\sim \xi$ [29] (Section 2) shows the suppression of exciton scattering in the IX condensate observed in the experiments. The suppression of scattering results in the suppression of the Dyakonov–Perel and Elliott–Yafet mechanisms of spin relaxation [80]. Furthermore, the spatial separation between an electron and a hole suppresses the Bir–Aronov–Pikus mechanism of spin relaxation for IXs [46, 81]. The suppression of these spin relaxation mechanisms results in a strong enhancement of the spin relaxation time in a condensate of IXs. While the spin relaxation times of free fermions—electrons and holes—can be short [81], the formation of a coherent gas of their boson pairs, IXs, results in a strong enhancement of their spin relaxation times, facilitating long-range spin currents.

The exciton polarization currents and associated spin textures are revealed by the polarization pattern of the emitted light measured by polarization-resolved imaging (Figs. 7c, 7d). The photoexcitation in these experiments was nonresonant and spatially separated

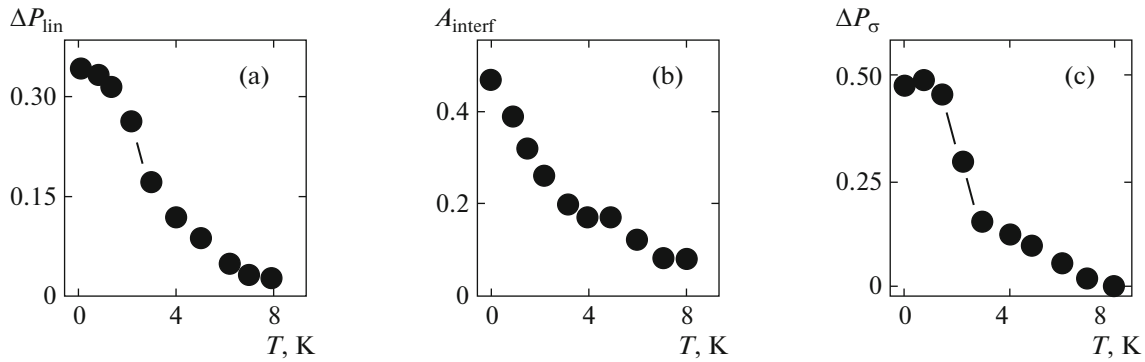


Fig. 8. (a) The amplitude of variation of the linear polarization of IX emission P_{lin} , (b) the interference visibility A_{interf} for $\delta x = 2 \mu\text{m}$, and (c) the amplitude of variation of the circular polarization of IX emission P_{σ} in the vortex of linear polarization vs temperature. From [31].

such that the exciton polarization was not induced by the pumping light.

The IXs in a GaAs CQW may have four spin projections on the z direction normal to the CQW plane: $J_z = -2, -1, +1, +2$. The states with $J_z = -1$ and $+1$ contribute to left- and right-circularly polarized emission and their coherent superposition to linearly polarized emission, whereas the states $J_z = -2$ and $+2$ are dark [81]. The electron and hole spin projections on the z axis are given by J_z , while in-plane projections of the electron and hole spins can be deduced from the exciton spin density matrix, which can be obtained from the measured polarization patterns [31].

The observed polarization patterns are qualitatively similar for both sources of cold excitons, the external ring and the LBS ring. The LBS ring is close to a model radially symmetric source of IXs with a divergent (hedgehog) momentum distribution (Fig. 7a). All LBS rings in the emission pattern show similar spin textures (Figs. 7c, 7d).

The binding energy released at the exciton formation in the rings and the current filament at the LBS center heat the exciton gas. The former heating source depletes the exciton condensate in the rings (Fig. 2g). The latter is so strong that the exciton gas is classical in the LBS ring center (Fig. 2c). The IXs cool down with increasing the distance r from the heating sources such that they can approach the condensation temperature at $r = r_0$ where the condensation is detected by an enhancement of the IX coherence length well beyond its classical value [29] (Figs. 2c, 2g, Section 2).

A ring of linear polarization is observed around the LBS center (Figs. 2d and 7c). This ring is observed in the region $r < r_0$, where the IX gas is classical (Figs. 2c, 2d). The linear polarization originates from the thermal distribution of IXs over the linearly polarized IX states. Heating the exciton gas by the current filament reduces the polarization degree in the LBS center and, as a result, leads to the appearance of a ring of linear polarization. No such polarization reduction is

observed in the MOES bead centers, which is consistent with the absence of heating by current filaments in the external ring area (Figs. 2h, 7c).

A helical exciton polarization texture that winds by 2π around the origin emerges in the LBS area at $r > r_0$ where the condensate forms (Figs. 2c, 2d, 7c). The IXs are generated in the LBS ring and travel out of the LBS origin (Fig. 7a). The exciton polarization is perpendicular to the exciton momentum. This produces a vortex of linear polarization. It emerges in concert with spontaneous coherence below the critical temperature (Fig. 8). The observed IX polarization currents are associated with spin currents carried by electrons and holes bound into IXs as is detailed below.

Applied magnetic fields bend the spin current trajectories, creating spiral patterns of linear polarization around the origin (Figs. 9a, 9b). The spiral direction of the exciton polarization current clearly deviates from the radial direction of the exciton density current. The control of the polarization patterns by a magnetic field shows that they are associated with spin.

Regular patterns are also observed in circular polarization (Fig. 7d). An LBS source of excitons generates a four-leaf pattern of circular polarization (Figs. 7d, 9c). This pattern vanishes with increasing the temperature (Fig. 8). An applied magnetic field transforms the four-leaf pattern of circular polarization to a bell-like pattern with a strong circular polarization in the center and polarization inversion a few micrometers away from the center (Figs. 9c, 9d).

Polarization patterns are also observed in the external ring region (Figs. 7c, 7d). At low temperatures, the MOES forms in the external ring. The MOES is characterized by a spatially ordered array of higher-density beads and is a condensate in momentum space [29] (Sections 2 and 3). The polarization texture in the external ring region appears as a superposition of the polarization textures produced by the MOES beads, with each being similar to the texture produced by an LBS. A periodic array of beads in the MOES (Fig. 7b)

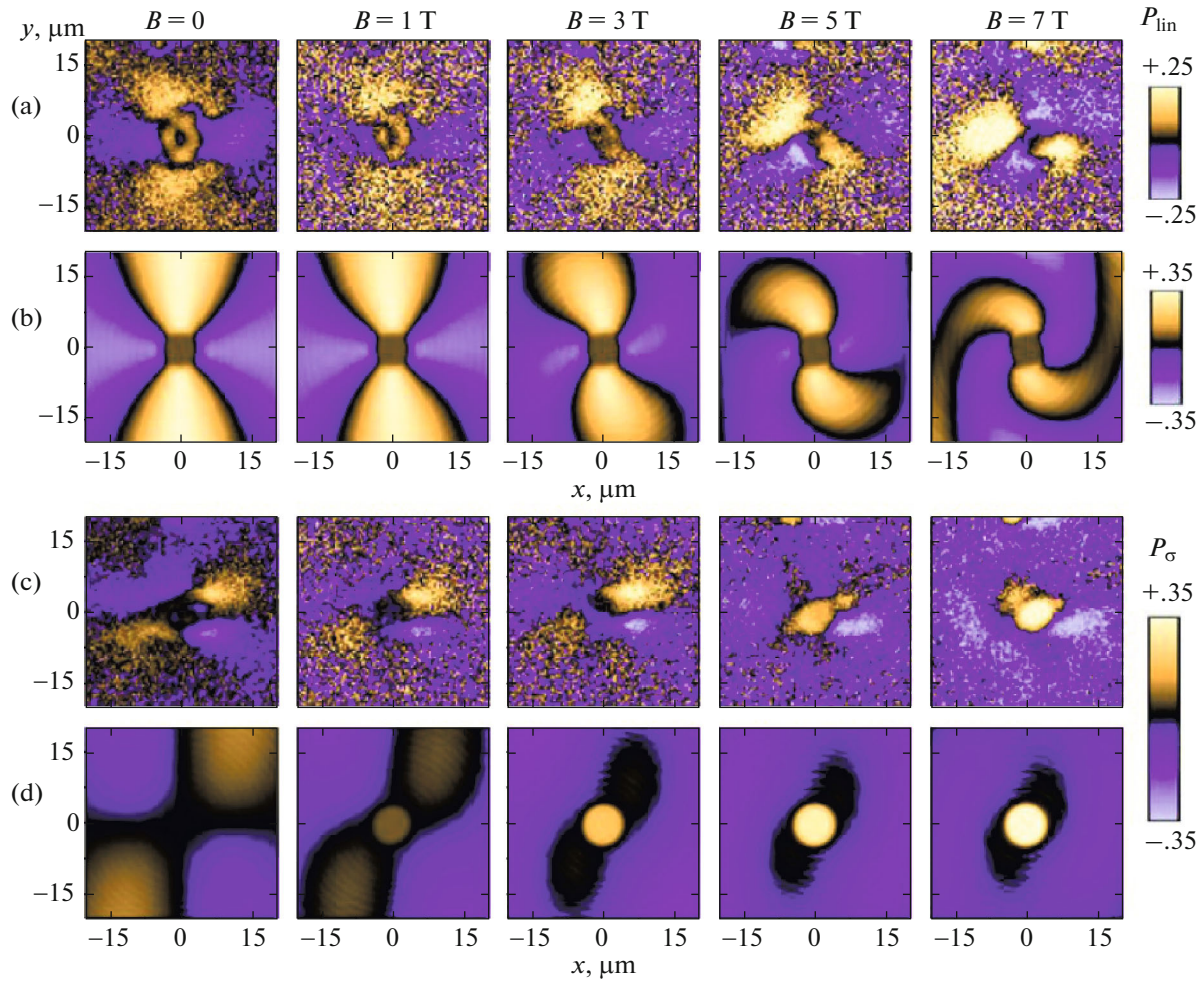


Fig. 9. (Color online) (a) Measured and (b) simulated patterns of linear polarization of the IX emission P_{lin} in the LBS region for different magnetic fields perpendicular to the QW plane B . (c) Measured and (d) simulated patterns of circular polarization of the IX emission P_{σ} in the region of LBS for different B . For all data, $T_{\text{bath}} = 0.1$ K; the LBS is at (105, 75) in Fig. 7c. From [31].

creates periodic polarization textures (Figs. 7c, 7d). The periodic polarization textures in the external ring region vanish above the critical temperature of the MOES [29].

The observed exciton polarization textures associated with the long-range spin currents carried by electrons and holes bound into bright and dark IX states are described by a theoretical model based on ballistic IX transport out of the LBS origin and coherent precession of spins of electrons and holes [31]. The former originates from the suppression of scattering and the latter from the suppression of spin relaxation in the condensate of IXs. The states with different spins are split due to the splitting of linearly polarized exciton states and spin-orbit (SO) interaction, which is described by the Dresselhaus Hamiltonian [82–84]. Exciton propagation out of the origin governed by this Hamiltonian results in the appearance of a vortex of linear polarization with the polarization perpendicular to the radial direction and a four-leaf pattern of circu-

lar polarization in $B = 0$, as well as spiral patterns of linear polarization and bell-like-with-inversion patterns of circular polarization in finite magnetic fields, qualitatively reproducing the main features of the experiment for both linear (Figs. 9a, 9b) and circular (Figs. 9c, 9d) polarizations [31].

This model describes the exciton polarization currents and allows deducing the spin currents carried by electrons and holes bound to excitons. It shows that both the electron and hole spin tend to align along the effective magnetic fields given by the Dresselhaus SO interaction [31].

5. EXCITONIC DEVICES

The IXs have a built-in dipole moment ed , where d is the separation between the electron and hole layers. For IXs in a CQW, d is close to the distance between the QW centers. The built-in dipole moment allows controlling IXs by voltage: an electric field F_z perpen-

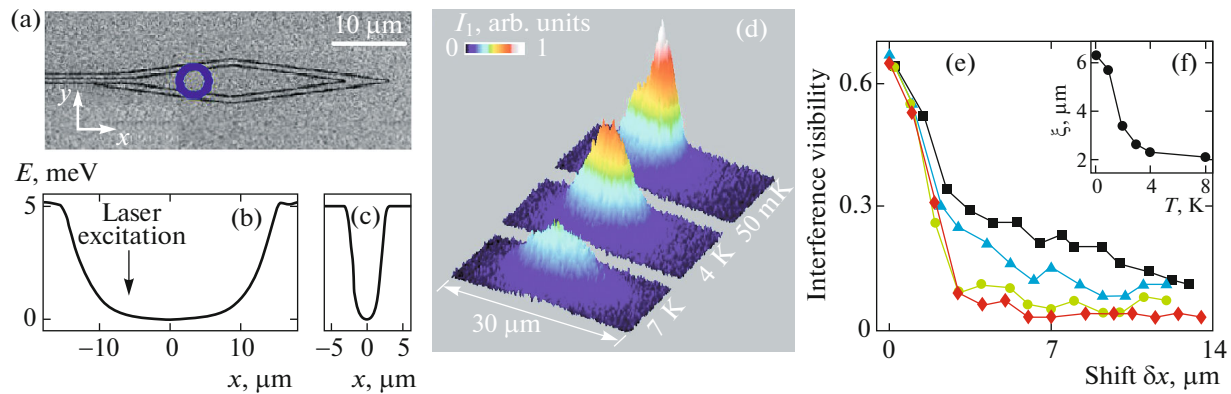


Fig. 10. (Color online) (a) SEM image of electrodes forming a diamond trap: a diamond-shaped electrode is surrounded by a thin wire electrode followed by an outer plane electrode. (b), (c) Simulation of the exciton energy profile through the trap center along (b) x and (c) y for $V_{\text{diamond}} = -2.5$ V, $V_{\text{wire}} = -2$ V, and $V_{\text{plane}} = -2$ V. The position of the laser excitation spot is indicated by the circle in (a) and by the arrow in (b). (d) IX emission patterns for $T_{\text{bath}} = 7$, 4, and 0.05 K. (e) $A_{\text{interf}}(\delta x)$ for IX in the trap for $T_{\text{bath}} = 50$ mK (black squares), 2 K (blue triangles), 4 K (green circles), and 8 K (red diamonds). (f) The IX coherence length ξ as a function of temperature. From [30].

pendicular to the QW plane results in the IX shift $E = -edF_z$ [85]. This allows creating in-plane potential landscapes for IXs, $E(x, y) = -edF_z(x, y)$. Advantages of electrostatically created potential landscapes include the opportunity to realize a desired potential profile and control it in situ by voltage. IXs were studied in various electrostatically created potential landscapes including ramps [47, 48], lattices [49–51], conveyers and stirring potentials [52, 53], traps [30, 54–63], and circuit devices [65]. We note that in-plane electric field F_r present near the electrode edges can lead to IX dissociation. Therefore, the CQW layers in our excitonic devices were positioned closer to the homogeneous bottom electrode. This design suppresses F_r , making the field-induced IX dissociation negligible [55].

5.1. Condensation of Excitons in a Trap

The confinement of atomic gases in traps has led to the realization of Bose–Einstein condensation of atoms [2, 3]. The detection of spontaneous coherence is a direct experimental measurement of condensation (Section 2). In this section, we overview the measurements of condensation and spontaneous coherence of IXs confined in an electrostatic trap [30]. In this work, we realized an electrostatic trap for IXs using a diamond-shaped electrode (Fig. 10a). Because a thinner electrode produces a smaller F_z due to the field divergence near the electrode edges, the diamond trap creates a confining potential with the IX energy gradually reducing toward the trap center (Figs. 10b, 10c) [30]. The excitons were generated by a 633 nm HeNe laser. The excitation beam was focused to a spot ~ 5 μm in diameter on a side of the trap (Figs. 10a, 10b). This excitation scheme allows further cooling the photoexcited excitons when they travel toward the trap center,

thus facilitating the realization of a cold IX gas in the trap. The first-order coherence function $g_1(\delta x)$ was measured by shift interferometry described in Section 2.

Figure 10d presents the temperature dependence of the IX emission pattern. At high temperatures, the IX cloud spreads over the trap, resulting in a broad spatial profile of the IX emission. With decreasing the temperature, IXs collect at the trap center (Fig. 10d). Studies of atoms in traps also show the collection of atoms at the trap center with lowering temperature due to the reduction of the thermal spreading of atoms over the trap and, eventually, condensation of atoms [2, 3].

To determine if IX condensation is realized in the trap, we performed shift-interferometry measurements. Figure 10e presents the amplitude of the interference fringes $A_{\text{interf}}(\delta x)$ for different temperatures. The spatial extension of $A_{\text{interf}}(\delta x)$ is characterized by a coherence length ξ at which the interference visibility drops by e times. A strong enhancement of the IX coherence length is observed at low temperatures (Fig. 10f). While ξ is considerably smaller than the IX cloud width at high temperatures, the entire IX cloud becomes coherent at low temperatures (Figs. 10d–10f).

In these experiments, the laser excitation energy exceeds the exciton energy by about 400 meV and the laser excitation spot is spatially separated from the interfering excitons. Therefore, the coherence studied in the IX gas is spontaneous coherence; it is not induced by coherence of the laser excitation. As discussed in Section 2, the coherence of an exciton gas is imprinted on the coherence of emission, which is described by the first-order coherence function $g_1(\delta x)$. In turn, this function is given by the amplitude of the interference fringes $A_{\text{interf}}(\delta x)$ in “the ideal experiment” with perfect spatial resolution. In real experi-

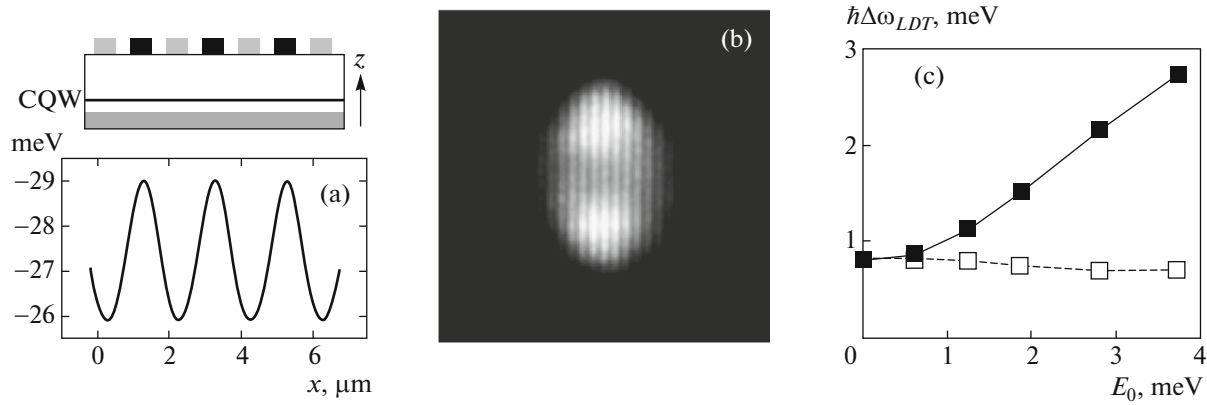


Fig. 11. (a) Schematic electrode pattern and the calculated lattice potential for IXs for the voltage modulation $\Delta V = 1$ V. (b) Emission image of IXs in a linear lattice. The applied voltage controls the lattice amplitude E_{lattice} . The laser excitation controls the IX density. (c) The interaction energy at the transition from the localized to delocalized regime as a function of E_{lattice} . Filled (open) squares present the data for the IX transport across (along) the lattice. From [50].

ments, the measured $A_{\text{interf}}(\delta x)$ is given by the convolution of $g_1(\delta x)$ with the PSF of the optical system used in the experiment [28].

For both a classical gas and a quantum gas, $g_1(\delta x)$ is close to 1 at $\delta x = 0$ and drops with increasing δx within the coherence length ξ . For a classical gas, ξ_{cl} is close to the thermal de Broglie wavelength λ_{dB} , which is well below the PSF width in the studied temperature range ($\xi_{\text{cl}} < \xi_{\text{cl}@0.1\text{K}} \sim 0.5 \mu\text{m}$, the PSF width is $\sim 2 \mu\text{m}$). Therefore, for a classical gas at temperatures above 4 K, the measured ξ is given by the PSF width (Figs. 10e, 10f).

In contrast, for a condensate, the coherence length becomes much longer than the thermal de Broglie wavelength and reaches the size of the exciton cloud in the trap, such that the entire exciton cloud becomes coherent. This signature of Bose–Einstein condensation is observed at the lowest temperatures in the experiment (Figs. 10d–10f). The measured transition temperature is ~ 2 K (Fig. 10f). Rough estimates of the temperature of the IX BEC in the trap are close to 2 K [30], while accurate estimates form the subject for future works.

5.2. Exciton Localization–Delocalization Transitions in Lattices and Random Potentials

Transport of particles in periodic potentials is a basic problem that concerns a variety of systems extending from condensed-matter systems with electrons in ion lattices to engineered systems such as photons in photon crystals and cold atoms in optical lattices. The particle localization and localization–delocalization transition (LDT) are among the basic transport phenomena. Particular cases of the LDT—the metal–insulator and superfluid–insulator transitions—have been studied for electrons, photons, and

cold atoms both in lattices and in random potentials [86–89].

In this section, we overview the measurements of IXs in electrostatic lattices [50]. In this system, as for cold atoms in lattices, parameters of both the lattice (e.g., the lattice amplitude) and the particles (e.g., the exciton density) can be controlled. Due to their long lifetimes, IXs can travel over large distances before recombining, which gives an opportunity to study exciton transport by imaging IX emission. The lattice potential for the IX $E(x)$ was created by interdigitated gates. Base voltage realized the indirect regime where the IXs are lower in energy than direct excitons, while a voltage modulation ΔV controlled the lattice amplitude [50]. An example of the calculated (unscreened) $E(x)$ is shown in Fig. 11a. The potential modulation is nearly sinusoidal, the lattice amplitude is controlled by ΔV , and the lattice period is determined by the electrode dimensions. The IX cloud extension is measured by IX emission imaging, an example is shown in Fig. 11b. The IX density is controlled by the excitation power P . At low P , the IX cloud profile essentially coincides with the laser excitation spot. This indicates that IXs do not travel beyond the excitation spot; i.e., they are localized. On the contrary, at high P , the IXs spread beyond the excitation spot, indicating that they are delocalized. The LDT with increasing the IX density is observed both without [26, 42] and with [50] the lattice. At the LDT, the exciton cloud starts to spread beyond the excitation spot, and the cloud extension changes from P -independent to increasing with P . The IX transport in the y direction along the linear lattice is only weakly affected by the lattice.

The IX energy increases with density due to the repulsive IX interaction. At large lattice amplitudes, the LDT occurs when the IX interaction energy is close to the lattice amplitude: $\hbar\Delta\omega_{\text{LDT}} \approx E_{\text{lattice}}$ (Fig. 11c). At the vanishing lattice amplitude, the

LDT occurs when the IX interaction energy is close to the amplitude of the random potential E_{rand} due to disorder. The latter forms mainly due to the QW width and alloy fluctuations in the structure.

We attribute the observed LDT to the interaction-induced percolation of the IX gas through the total external potential $E_{\text{tot}}(\mathbf{r})$, which is the sum of the periodic lattice potential $E_{\text{lattice}}(x)$ and the random potential $E_{\text{rand}}(\mathbf{r})$. If the local exciton density $n(\mathbf{r})$ is low, IXs are concentrated in the minima of the potential $E_{\text{tot}}(\mathbf{r})$. As a result, the exciton transport from one potential minimum to the next via thermal activation or quantum tunneling is exponentially slow. As the IX average density increases and reaches a certain threshold—“percolation point”—the potential is screened by the interacting IXs, which permits a faster exciton transport, i.e., the observed delocalization. This scenario naturally leads to $\hbar\Delta\omega_{\text{LDT}} \approx E_{\text{tot}}$, which reduces to $\hbar\Delta\omega_{\text{LDT}} \approx E_{\text{lattice}}$ and $\hbar\Delta\omega_{\text{LDT}} \approx E_{\text{rand}}$ for large and small lattice amplitude, respectively [50].

A similar LDT was observed for IXs in two-dimensional electrostatic lattices [51]. Two-dimensional electrostatic lattices were realized using patterned interdigitated electrodes. This method allows creating a variety of artificial lattices, which can be controlled in situ: lattice structure is set by the electrode pattern, and the depth of the lattice potential is controlled by applied voltages [51].

We also observed a dynamic localization-delocalization transition (DLDT) for IXs in moving lattices—conveyers [52]. The conveyers for IXs were created by a set of ac voltages applied to the electrodes on the sample surface. The wavelength of this moving lattice is set by the electrode periodicity, the amplitude is controlled by the applied voltage, and the velocity is controlled by the ac frequency. The excitonic conveyer realizes controlled transport of excitons as CCDs realize controlled transport of electrons. For a shallow conveyer, the IXs do not follow the moving lattice, i.e., are dynamically delocalized in the lattice. In contrast, at higher conveyer amplitudes, IXs are moved by the moving lattice, i.e., are dynamically localized in the lattice. At the DLDT, the exciton cloud starts to follow the conveyer. We studied the DLDT dependence on the IX density and the conveyer amplitude and velocity [52]. As in the case of the LDT in static lattices [50, 51], the origin of DLDT in moving lattices is associated with screening by interacting IXs of the disorder and lattice potentials, which, in the conveyer case, are static and moving, respectively [52]. A similar DLDT was observed in stirring potentials for IXs [53].

The lattice potential causes periodic modulations of the IX emission energy and intensity. These modulations were used in [50] to estimate correlations in the IX system. The estimates show that correlations result in a substantial reduction of the IX repulsive interaction in comparison to the mean-field Hartree approximation. The lattices provide a tool for experimental

studies of correlations, which is a subject for future works.

6. SUMMARY

In this contribution, we briefly overview our studies of collective phenomena in cold indirect excitons over the past decade, presenting spontaneous coherence and condensation of excitons, spatially modulated exciton state, long-range spin currents and spin textures, and exciton localization-delocalization transitions.

ACKNOWLEDGMENTS

I am grateful to L.V. Keldysh for the inspiring discussions. Our studies of indirect excitons presented in this contribution were performed in collaboration with G. Abstreiter, P. Andreakou, G.O. Andreev, G. Böhm, E.V. Calman, K.L. Campman, D.S. Chemla, C.J. Dorow, A.I. Filin, M.M. Fogler, N.A. Gippius, A.C. Gossard, J.C. Graves, A.A. Guenther, A.T. Hammack, M. Hanson, M.W. Hasling, A.A. High, A.L. Ivanov, A.V. Kavokin, Y.Y. Kuznetsova, J.R. Leonard, L.S. Levitov, T.C.H. Liew, P.B. Littlewood, A.D. Meyertholen, A.V. Mintsev, L. Mouchlidis, T. Ostatnický, M. Remeika, B.D. Simons, L.E. Smallwood, M. Vladimirova, G. Weimann, J. Wilkes, A.G. Winbow, Sen Yang, and A. Zrenner, and it is a pleasure to thank my collaborators. Our studies of indirect excitons are supported by the DOE Office of Basic Energy Sciences under award DE-FG02-07ER46449 and by NSF DMR award 1407277.

REFERENCES

1. L. V. Keldysh and A. N. Kozlov, *Sov. Phys. JETP* **27**, 521 (1968).
2. E. A. Cornell and C. E. Wieman, *Rev. Mod. Phys.* **74**, 875 (2002).
3. W. Ketterle, *Rev. Mod. Phys.* **74**, 1131 (2002).
4. L. V. Keldysh and Yu. V. Kopaev, *Sov. Phys. Solid State* **6**, 2219 (1965).
5. D. Yoshioka and A. H. MacDonald, *J. Phys. Soc. Jpn.* **59**, 4211 (1990).
6. X. M. Chen and J. J. Quinn, *Phys. Rev. Lett.* **67**, 895 (1991).
7. L. V. Keldysh, *Contemp. Phys.* **27**, 395 (1986).
8. D. Hulin, A. Mysyrowicz, and C. B. á la Guillaume, *Phys. Rev. Lett.* **45**, 1970 (1980).
9. I. V. Kukushkin, V. D. Kulakovskii, and V. B. Timofeev, *JETP Lett.* **34**, 34 (1981).
10. D. W. Snoke, J. P. Wolfe, and A. Mysyrowicz, *Phys. Rev. Lett.* **64**, 2543 (1990).
11. A. E. Bulatov and S. G. Tikhodeev, *Phys. Rev. B* **46**, 15058 (1992).
12. E. Fortin, S. Fafard, and A. Mysyrowicz, *Phys. Rev. Lett.* **70**, 3951 (1993).

13. S. G. Tikhodeev, G. A. Kopelevich, and N. A. Gippius, *Phys. Status Solidi B* **206**, 45 (1998).
14. K. E. O'Hara, L. O. Suilleabhain, and J. P. Wolfe, *Phys. Rev. B* **60**, 10565 (1999).
15. N. Naka and N. Nagasawa, *Phys. Status Solidi B* **238**, 397 (2003).
16. K. Yoshioka, Y. Morita, K. Fukuoka, and M. Kuwata-Gonokami, *Phys. Rev. B* **88**, 041201(R) (2013).
17. Yu. E. Lozovik and V. I. Yudson, *Sov. Phys. JETP* **44**, 389 (1976).
18. S. I. Shevchenko, *Sov. J. Low Temp. Phys.* **2**, 251 (1976).
19. T. Fukuzawa, S. S. Kano, T. K. Gustafson, and T. Ogawa, *Surf. Sci.* **228**, 482 (1990).
20. J. Feldmann, G. Peter, E. O. Göbel, P. Dawson, K. Moore, C. Foxon, and R. J. Elliott, *Phys. Rev. Lett.* **59**, 2337 (1987).
21. L. C. Andreani, F. Tassone, and F. Bassani, *Solid State Commun.* **77**, 641 (1991).
22. B. Deveaud, F. Clerot, N. Roy, K. Satzke, B. Sermage, and D. S. Katzer, *Phys. Rev. Lett.* **67**, 2355 (1991).
23. S. G. Tikhodeev, *Sov. Phys. JETP* **70**, 380 (1990).
24. A. L. Ivanov, P. B. Littlewood, and H. Haug, *Phys. Rev. B* **59**, 5032 (1999).
25. L. V. Butov, A. L. Ivanov, A. Imamoglu, P. B. Littlewood, A. A. Shashkin, V. T. Dolgoplov, K. L. Campman, and A. C. Gossard, *Phys. Rev. Lett.* **86**, 5608 (2001).
26. L. V. Butov, A. C. Gossard, and D. S. Chemla, *Nature* **418**, 751 (2002).
27. Sen Yang, A. T. Hammack, M. M. Fogler, L. V. Butov, and A. C. Gossard, *Phys. Rev. Lett.* **97**, 187402 (2006).
28. M. M. Fogler, Sen Yang, A. T. Hammack, L. V. Butov, and A. C. Gossard, *Phys. Rev. B* **78**, 035411 (2008).
29. A. A. High, J. R. Leonard, A. T. Hammack, M. M. Fogler, L. V. Butov, A. V. Kavokin, K. L. Campman, and A. C. Gossard, *Nature* **483**, 584 (2012).
30. A. A. High, J. R. Leonard, M. Remeika, L. V. Butov, M. Hanson, and A. C. Gossard, *Nano Lett.* **12**, 2605 (2012).
31. A. A. High, A. T. Hammack, J. R. Leonard, Sen Yang, L. V. Butov, T. Ostatnický, M. Vladimirova, A. V. Kavokin, T. C. H. Liew, K. L. Campman, and A. C. Gossard, *Phys. Rev. Lett.* **110**, 246403 (2013).
32. M. Alloing, M. Beian, M. Lewenstein, D. Fuster, Y. González, L. González, R. Combescot, M. Combescot, and F. Dubin, *Europhys. Lett.* **107**, 10012 (2014).
33. D. Nandi, A. D. K. Finck, J. P. Eisenstein, L. N. Pfeiffer, and K. W. West, *Nature* **488**, 481 (2012).
34. L. V. Butov, A. Zrenner, G. Abstreiter, G. Böhm, and G. Weimann, *Phys. Rev. Lett.* **73**, 304 (1994).
35. L. V. Butov and A. I. Filin, *Phys. Rev. B* **58**, 1980 (1998).
36. I. B. Spielman, J. P. Eisenstein, L. N. Pfeiffer, and K. W. West, *Phys. Rev. Lett.* **84**, 5808 (2000).
37. J. P. Eisenstein and A. H. MacDonald, *Nature* **432**, 691 (2004).
38. E. Tutuc, M. Shayegan, and D. A. Huse, *Phys. Rev. Lett.* **93**, 036802 (2004).
39. L. Tiemann, J. G. S. Lok, W. Dietsche, K. von Klitzing, K. Muraki, D. Schuh, and W. Wegscheider, *Phys. Rev. B* **77**, 033306 (2008).
40. B. Karmakar, V. Pellegrini, A. Pinczuk, L. N. Pfeiffer, and K. W. West, *Phys. Rev. Lett.* **102**, 036802 (2009).
41. Sen Yang, L. V. Butov, B. D. Simons, K. L. Campman, and A. C. Gossard, *Phys. Rev. B* **91**, 245302 (2015).
42. A. L. Ivanov, L. E. Smallwood, A. T. Hammack, Sen Yang, L. V. Butov, and A. C. Gossard, *Europhys. Lett.* **73**, 920 (2006).
43. L. V. Butov, L. S. Levitov, A. V. Mintsev, B. D. Simons, A. C. Gossard, and D. S. Chemla, *Phys. Rev. Lett.* **92**, 117404 (2004).
44. Sen Yang, A. V. Mintsev, A. T. Hammack, L. V. Butov, and A. C. Gossard, *Phys. Rev. B* **75**, 033311 (2007).
45. Sen Yang, L. V. Butov, L. S. Levitov, B. D. Simons, and A. C. Gossard, *Phys. Rev. B* **81**, 115320 (2010).
46. J. R. Leonard, Y. Y. Kuznetsova, S. Yang, L. V. Butov, T. Ostatnický, A. Kavokin, and A. C. Gossard, *Nano Lett.* **9**, 4204 (2009).
47. M. Hagn, A. Zrenner, G. Böhm, and G. Weimann, *Appl. Phys. Lett.* **67**, 232 (1995).
48. A. Gärtner, A. W. Holleitner, J. P. Kotthaus, and D. Schuh, *Appl. Phys. Lett.* **89**, 052108 (2006).
49. S. Zimmermann, G. Schedelbeck, A. O. Govorov, A. Wixforth, J. P. Kotthaus, M. Bichler, W. Wegscheider, and G. Abstreiter, *Appl. Phys. Lett.* **73**, 154 (1998).
50. M. Remeika, J. C. Graves, A. T. Hammack, A. D. Meyertholen, M. M. Fogler, L. V. Butov, M. Hanson, and A. C. Gossard, *Phys. Rev. Lett.* **102**, 186803 (2009).
51. M. Remeika, M. M. Fogler, L. V. Butov, M. Hanson, and A. C. Gossard, *Appl. Phys. Lett.* **100**, 061103 (2012).
52. A. G. Winbow, J. R. Leonard, M. Remeika, Y. Y. Kuznetsova, A. A. High, A. T. Hammack, L. V. Butov, J. Wilkes, A. A. Guenther, A. L. Ivanov, M. Hanson, and A. C. Gossard, *Phys. Rev. Lett.* **106**, 196806 (2011).
53. M. W. Hasling, Y. Y. Kuznetsova, P. Andreakou, J. R. Leonard, E. V. Calman, C. J. Dorow, L. V. Butov, M. Hanson, and A. C. Gossard, *J. Appl. Phys.* **117**, 023108 (2015).
54. T. Huber, A. Zrenner, W. Wegscheider, and M. Bichler, *Phys. Status Solidi A* **166**, R5 (1998).
55. A. T. Hammack, N. A. Gippius, Sen Yang, G. O. Andreev, L. V. Butov, M. Hanson, and A. C. Gossard, *J. Appl. Phys.* **99**, 066104 (2006).
56. G. Chen, R. Rapaport, L. N. Pfeiffer, K. West, P. M. Platzman, S. Simon, Z. Vörös, and D. Snoke, *Phys. Rev. B* **74**, 045309 (2006).
57. A. V. Gorbunov and V. B. Timofeev, *JETP Lett.* **84**, 329 (2006).
58. A. V. Gorbunov and V. B. Timofeev, *JETP Lett.* **96**, 138 (2012).
59. A. V. Gorbunov and V. B. Timofeev, *Solid State Commun.* **157**, 6 (2013).
60. A. A. High, A. T. Hammack, L. V. Butov, L. Mouchliadis, A. L. Ivanov, M. Hanson, and A. C. Gossard, *Nano Lett.* **9**, 2094 (2009).

61. G. J. Schinner, J. Repp, E. Schubert, A. K. Rai, D. Reuter, A. D. Wieck, A. O. Govorov, A. W. Holleitner, and J. P. Kotthaus, *Phys. Rev. Lett.* **110**, 127403 (2013).
62. G. J. Schinner, J. Repp, E. Schubert, A. K. Rai, D. Reuter, A. D. Wieck, A. O. Govorov, A. W. Holleitner, and J. P. Kotthaus, *Phys. Rev. B* **87**, 205302 (2013).
63. Y. Shilo, K. Cohen, B. Laikhtman, K. West, L. Pfeiffer, and R. Rapaport, *Nature Commun.* **4**, 2335 (2013).
64. M. Stern, V. Umansky, and I. Bar-Joseph, *Science* **343**, 55 (2014).
65. P. Andreakou, S. V. Poltavtsev, J. R. Leonard, E. V. Calman, M. Remeika, Y. Y. Kuznetsova, L. V. Butov, J. Wilkes, M. Hanson, and A. C. Gossard, *Appl. Phys. Lett.* **104**, 091101 (2014).
66. D. E. Nikonov and A. Imamoglu, arXiv:quant-ph/9806003.
67. S. R. E. Yang, Q. H. Park, and J. Yeo, *Int. J. Mod. Phys. B* **18**, 3797 (2004).
68. L. S. Levitov, B. D. Simons, and L. V. Butov, *Phys. Rev. Lett.* **94**, 176404 (2005).
69. A. A. Chernyuk and V. I. Sugakov, *Phys. Rev. B* **74**, 085303 (2006).
70. A. V. Paraskevov and T. V. Khabarova, *Phys. Lett. A* **368**, 151 (2007).
71. C. S. Liu, H. G. Luo, and W. C. Wu, *Phys. Rev. B* **80**, 125317 (2009).
72. J. Wilkes, E. A. Muljarov, and A. L. Ivanov, *Phys. Rev. Lett.* **109**, 187402 (2012).
73. S. V. Andreev, *Phys. Rev. Lett.* **110**, 146401 (2013).
74. S. V. Andreev, A. A. Varlamov, and A. V. Kavokin, *Phys. Rev. Lett.* **112**, 036401 (2014).
75. R. Rapaport, G. Chen, D. Snoke, S. H. Simon, L. Pfeiffer, K. West, Y. Liu, and S. Denev, *Phys. Rev. Lett.* **92**, 117405 (2004).
76. G. Chen, R. Rapaport, S. H. Simon, L. Pfeiffer, and K. West, *Phys. Rev. B* **71**, 041301(R) (2005).
77. M. Haque, *Phys. Rev. E* **73**, 066207 (2006).
78. X. Zhu, P. B. Littlewood, M. Hybertsen, and T. M. Rice, *Phys. Rev. Lett.* **74**, 1633 (1995).
79. Yu. E. Lozovik and O. L. Berman, *JETP Lett.* **64**, 573 (1996).
80. M. I. Dyakonov, *Spin Physics in Semiconductors* (Springer, New York, 2008).
81. M. Z. Maialle, E. A. de Andrada e Silva, and L. J. Sham, *Phys. Rev. B* **47**, 15776 (1993).
82. E. I. Rashba and E. Ya. Sherman, *Phys. Lett. A* **129**, 175 (1988).
83. C. Wu and I. Mondragon-Shem, arXiv:0809.3532v1.
84. J.-W. Luo, A. N. Chantis, M. van Schilfgaarde, G. Bester, and A. Zunger, *Phys. Rev. Lett.* **104**, 066405 (2010).
85. D. A. B. Miller, D. S. Chemla, T. C. Damen, A. C. Gossard, W. Wiegmann, T. H. Wood, and C. A. Burrus, *Phys. Rev. B* **32**, 1043 (1985).
86. P. A. Lee and T. V. Ramakrishnan, *Rev. Mod. Phys.* **57**, 287 (1985).
87. D. S. Wiersma, P. Bartolini, A. Lagendijk, and R. Righini, *Nature* **390**, 671 (1997).
88. M. Greiner, O. Mandel, T. Esslinger, T. W. Hänsch, and I. Bloch, *Nature* **415**, 39 (2002).
89. J. Billy, V. Josse, Z. Zuo, A. Bernard, B. Hambrecht, P. Lugan, D. Clement, L. Sanchez-Palencia, P. Bouyer, and A. Aspect, *Nature* **453**, 891 (2008).